Front. Chem. Sci. Eng. 2022, 16(3): 420–432
https://doi.org/10.1007/s11705-021-2065-7

RESEARCH ARTICLE

Tripotassium citrate monohydrate derived carbon nanosheets as a competent assistant to manganese dioxide with remarkable performance in the supercapacitor

Wenjing Zhang[1], Xiaoxue Yuan[1], Xuehua Yan (✉)[1,2], Mingyu You[1], Hui Jiang[1], Jieyu Miao[1], Yanli Li[1], Wending Zhou[1], Yihan Zhu[1], Xiaonong Cheng[1]

1 School of Materials Science and Engineering, Jiangsu University, Zhenjiang 212013, China
2 Institute for Advanced Materials, Jiangsu University, Zhenjiang 212013, China

Abstract Production cost, capacitance, and electrode materials safety are the key factors to be concerned about for supercapacitors. In this work, a type of carbon nanosheets was produced through the carbonization of tripotassium citrate monohydrate and nitric acidification. Subsequently, a well-designed manganese dioxide/carbon nanosheets composite was synthesized through hydrothermal treating. The carbon nanosheets served as the substrate for growing the manganese dioxide, regulating its distribution, and preventing it from inhomogeneous dimensions and severe agglomeration. Many manganese dioxide nanosheets grew vertically on the numerous functional groups generated on the surface of the carbon nanosheets during acidification. The synergistic combination of carbon nanosheets and manganese dioxide tailors the electrochemical performance of the composite, which benefits from the excellent conductivity and stability of carbon nanosheets. The carbon nanosheets derived from tripotassium citrate monohydrate are conducive to the remarkable performance of manganese dioxide/carbon nanosheets electrode. Finally, an asymmetric supercapacitor with active carbon as the cathode and manganese dioxide/carbon nanosheets as the anode was assembled, achieving an outstanding energy density of 54.68 $Wh \cdot kg^{-1}$ and remarkable power density of 6399.2 $W \cdot kg^{-1}$ superior to conventional lead-acid batteries. After 10000 charge-discharge cycles, the device retained 75.3% of the initial capacitance, showing good cycle stability. Two assembled asymmetric supercapacitors in series charged for 3 min could power a yellow light emitting diode with an operating voltage of 2 V for 2 min. This study may provide valuable insights for applying carbon materials and manganese dioxide in the energy storage field.

Keywords carbon nanosheets, manganese dioxide, asymmetric supercapacitors, energy density, power density

1 Introduction

The development of energy storage devices, such as batteries and supercapacitors, tends towards miniaturization, portability, and transparency. However, the energy density and the power density of energy storage devices must be considered for practical applications. Conventional lead-acid batteries could meet the challenges of low energy density and power density applications [1]. Lithium-ion batteries offer higher capacitance, energy density, and power density than lead-acid batteries. Nevertheless, dendrites on the surface of electrodes could cause the lithium-ion batteries to explode [2]. Supercapacitors have been extensively studied due to their remarkable portability, acceptable production cost, and outstanding stability.

The energy density and the power density of energy storage devices could be calculated with the following equations [3]:

$$E = \frac{1}{2}C(\Delta V)^2, \tag{1}$$

$$P = E/T, \tag{2}$$

where the energy density E is determined by the specific capacitance C and operating potential window ΔV of the electrode materials, and power density P is determined by energy density and discharge period T. Both E and P could

Received December 22, 2020; accepted April 15, 2021

E-mail: xhyan@mail.ujs.edu.cn

be increased with transition metal oxides including RuO_2, Fe_2O_3, Co_3O_4, and NiO_2 as the supercapacitor electrodes because of their excellent pseudo-capacitance via fast and reversible Faradic redox processes [4–6]. The production cost of RuO_2 electrodes is high though they hold the highest capacitance. Meanwhile, magnetic substances, such as Fe_2O_3, Co_3O_4, and NiO_2, could contaminate the instruments when they are characterized. As one of the pseudocapacitive materials, MnO_2 could be an appropriate electrode material offering prominent specific capacitance and various crystal structures [7], ensuring an effective ion diffusion essential for high energy density and power density. Wang et al. prepared a series of supercapacitor electrodes based on MnO_2 composites, mainly from biomass materials [8–12]. Nevertheless, many reported MnO_2 electrodes have nonuniform dimensions and severe agglomeration that weaken their electrochemical performance [13]. Meanwhile, the cycle stability of MnO_2 electrodes can not meet the demand of practical applications due to ordinary electrical conductivity and the expansion/contraction of crystal lattice during cycle testing [14,15].

Nontoxic nano-scale carbon materials with excellent electrical conductivity, such as reduced graphene oxide (rGO) [16], carbon nanotubes (CNTs) [17], carbon nanofibers [18], and carbon quantum dots (CQDs) [19], have been explored to solve the problems with MnO_2 electrodes. Zhou et al. [16] synthesized an asymmetric supercapacitor (ASC) using rGO/MnO_2/polypyrrole ternary film, which exhibited a fascinating potential window of 1.7 V with outstanding cycle stability of 93% after 8000 cycles. Prasath et al. [19] prepared a CQD@MnO_2 electrode through the hydrothermal method and carbonization, which showed an extraordinary specific capacitance with an excellent rate capability due to the CQD networks' great specific surface area and effective influence on electroconductivity. Compared with other carbon electrodes, carbon nanosheets (CNSs) are suitable for synthesizing MnO_2 due to their low cost and simplicity [20]. CNS is two-dimensional compared to particulate (0D) or linear (1D) electrode materials [21], which could facilitate large-quantity MnO_2 formation on the electrode and enhance the performance of MnO_2 composites.

In this work, a low-cost, novel electrode material based on MnO_2/CNS was prepared. After the carbonization of tripotassium citrate monohydrate and HNO_3 acidification, an active CNS was produced for the uniform growth of MnO_2 on its surface, eliminating MnO_2 granules with nonuniform dimensions and severe agglomeration. The activation of HNO_3 produced large quantities of functional groups for the combination of CNS and MnO_2 nanosheets, which provided plenty of transferring and reacting sites for ions from the electrolyte and promoted the electrochemical performance of the composite. The carbon materials offered excellent conductivity and stability under strong current; thus, the composite showed much better rate capability. An ASC was successfully assembled with purchased active carbon (AC) as the cathode and MnO_2/CNS as the anode, which showed excellent energy density and power density superior to conventional lead-acid batteries. The supercapacitor exhibited good cycle stability after 10000 charge-discharge cycles. Two of the assembled ASCs in series could power a yellow light emitting diode (LED) with an operating voltage of 2 V.

2 Experimental

2.1 Materials

Tripotassium citrate monohydrate ($K_3C_6H_5O_7 \cdot H_2O$), $KMnO_4$(AC), KOH (AC), hydrochloric acid (38%), C_2H_5OH (95%), and HNO_3 (68%) were purchased from Zhenjiang Yinhai Co., Ltd. and Sinopharm Chemical Reagent Co., Ltd. Deionized water was produced in the laboratory.

2.2 CNS preparation

CNS was produced through carbonization. In a nitrogen atmosphere, 5 g of $K_3C_6H_5O_7 \cdot H_2O$ was gradually heated to 800 °C at 5 °C $\cdot$ min^{-1} and maintained at 800 °C for 2 h. The obtained powder was purified 4 to 5 times in a centrifuge with 30 mL HCl (1 mol $\cdot$ L^{-1}) solution to remove impurities. Then, the powder was put into a beaker containing 50 mL HNO_3 (5 mol $\cdot$ L^{-1}) and stirred for 12 h at 75 °C to produce functional groups on the surface. Finally, the products were rinsed three times with 20 mL ethanol and another three times with 20 mL deionized water before dried in a vacuum oven at 60 °C over 12 h for the subsequent synthesis of the MnO_2/CNS composite.

2.3 MnO_2/CNS composite synthesis

The MnO_2/CNS composite was prepared by the hydrothermal method from a previous study [22]. First, 20 mg of CNS was immersed into 30 mL deionized water and dispersed through ultrasonic treatment for 20 min. Second, 0.316 g (0.002 mol) $KMnO_4$ and 1 mL (2 mol $\cdot$ L^{-1}) HCl were alternately added into the solution and stirred at room temperature for another 1 h. Subsequently, the mixture was transferred into a 100 mL Teflon-lined stainless steel autoclave and kept at 90 °C for 2 h. Then, the products were rinsed several times in a centrifuging with 10 mL ethanol and several times with 10 mL deionized water. After drying in a vacuum oven at 65 °C for 10 h, the MnO_2/CNS composite was obtained. The schematic diagram for the preparation of MnO_2/CNS is presented in Fig. 1. According to a similar method, pure MnO_2 was synthesized without the introduction of CNS.

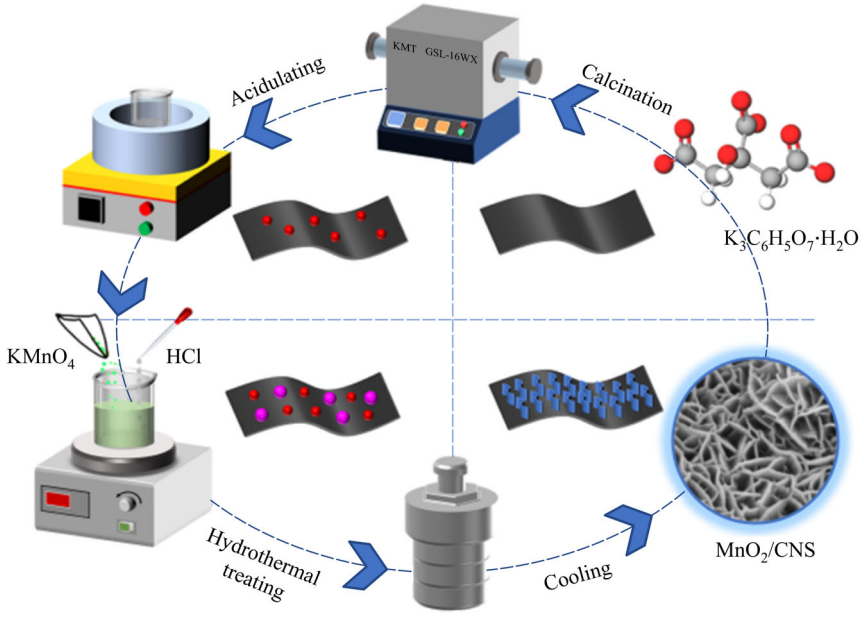

Fig. 1 Schematic diagram for the preparation of MnO_2/CNS.

2.4 Characterization

The crystal structure of the obtained materials was observed via X-ray diffraction (XRD, D8 ADVANCE) with Cu Kα radiation ($\lambda = 0.153$ nm) scanning from 15° to 75° at 4°·min^{-1}. A Raman microscope (LabRam HR Evolution, wavelength of 531 nm) was used to produce the Raman spectra of the obtained products. The valence states of the composite elements were explored via X-ray photoelectron spectroscopy (XPS, Thermo ESCALAB 250XI) with the excitation of Al Kα radiation at 1486.8 eV. Scanning electron microscopy (SEM, Zeiss Gemini 300), transmission electron microscopy (TEM, FEI Talos F200X), atomic force microscope (AFM, Bruker Dimension ICON), and energy-dispersive X-ray spectroscopy (EDS) were used to observe the thickness of CNS, the morphologies of the products, and the distributions of elements in the composite, respectively.

2.5 Electrochemical analysis

A three-electrode system was adopted on a CHI760E electrochemical workstation to evaluate the obtained products' electrochemical performance. Cyclic voltammetry testing (CV), galvanostatic charge/discharge testing (GCD), and electrochemical impedance spectroscopy (EIS) testing were performed. In the three-electrode system, the working electrode was the obtained product, the reference electrode was a cylindrical Ag/AgCl electrode, and the counter electrode was a 1 cm × 1 cm platinum flake. The electrolyte was 3 mol·L^{-1} KOH, and the working electrode was soaked in the electrolyte for 5 h before testing for sufficient ion infiltration. The specific capacitance of the working electrode can be calculated with the following equation [22]:

$$C = \frac{Q}{\Delta V}, \tag{3}$$

where Q represents the total discharging charge of the working electrode, and ΔV represents the potential window in the charging and discharging process of the working electrode. The specific capacitance can be calculated with the following equation [22]:

$$C_M = \frac{I}{M}\frac{\Delta t}{\Delta V} \text{ or } C_S = \frac{I}{S}\frac{\Delta t}{\Delta V}, \tag{4}$$

where I is the current magnitude of the charging and discharging process, Δt represents the discharging period of the working electrode, ΔV is the potential window in the charging and discharging process, and M and S are the loading and coverage of the working electrode, respectively. The mass loading of CNS, MnO_2, and MnO_2/CNS were 1.85, 1.77, and 2.02 mg·cm^{-2}, respectively.

3 Results and discussion

3.1 Morphologies and compositions

Figure 2 presents the results of XRD, Raman spectra, and XPS for CNS and MnO_2/CNS. Two diffraction peaks at 28.01° and 42.02° in Fig. 2(a) are verified as the (002) and (004) planes of the graphitic carbon [23]. For MnO_2/CNS, six peaks at 21.81°, 36.84°, 42.05°, 55.29°, 59.93°, and 66.17° are indexed to the (101), (210), (211), (212), (312),

and (412) planes of MnO_2, which is birnessite-type (JCPDS No.39-0375) [24,25]. Due to the intensive peaks of MnO_2 in the composite, the CNS peaks are too slight to find. Raman and XPS evaluations were performed to verify the existence of CNS peaks and the combination between CNS and MnO_2. Two strong peaks at 1347 and 1576 cm^{-1}, representing the D-band and G-band for graphitic carbons, respectively [26], are emerged in CNS and MnO_2/CNS, which prove the existence of CNS in the composite. Three major peaks at 493, 551, and 645 cm^{-1} of MnO_2 can be observed in MnO_2/CNS. The peak at 645 cm^{-1} corresponds to the crystal structure of MnO_2 formed orderly in a broad area [27]. Figures 2(c)–2(f) exhibit the XPS results of MnO_2/CNS for evaluating the valence states of different elements in the composite. Figure 2(c) shows four distinct peaks from 284.04 to 653.01 eV, indicating the Mn, O, and C elements in the composite. As shown in Fig. 2(d), the peak at 284.08 eV signifies the C–C and C = C bonds of CNS [28]. Two weak peaks at 285.28 and 287.88 eV represent the C–O and C = O bonds, respectively, derived from HNO_3 acidification during CNS synthesis [28]. The slight peak at 282.78 eV can be ascribed to the C–Mn bond formed in the hydrothermal process. The peak at 529.08 eV in Fig. 2(e) represents the Mn–O–Mn bond. Two minor peaks at 530.48 and 532.18 eV represent the C–O–C and C = O bond [28]. The characteristic valence state of the manganese is shown in Fig. 2(f). The binding energy space between $Mn2p_{3/2}$ at 641.58 eV and $Mn2p_{1/2}$ at 653.18 eV is 11.5 eV, prominently demonstrating that the original manganese valence state in the composite is Mn^{4+} [29]. The other peaks of Mn at 644.38, 648.58, and 656.48 eV correspond to a small quantity of Mn^{3+} and Mn^{2+} originated from the hydrothermal reaction.

Figure 3 shows the SEM images of acidless-treated CNS, active CNS, MnO_2 granules, and MnO_2/CNS. As shown in Figs. 3(a) and 3(b), CNS produced through the carbonization of $K_3C_6H_5O_7 \cdot H_2O$ and sufficient HNO_3 acidification is more dispersive and rough than those produced through the direct carbonization of $K_3C_6H_5O_7 \cdot H_2O$. Unlike the MnO_2 granules (Fig. 3(c)) with ununiform dimensions that are synthesized without active CNS, the MnO_2 nanosheets are vertically assembled on CNS (Fig. 3(d)), demonstrating a more homogeneous distribution in the composite ascribed to the active CNS advantages in the formation and growth of MnO_2 nanosheets.

Figure 4 shows the TEM images of active CNS and MnO_2/CNS, the 3D AFM image of active CNS, and the thickness curve of active CNS. Figure 4(a) illustrates that CNS is a two-dimensional material. Compared to raw CNS, significantly more MnO_2 nanosheets synthesized through hydrothermal treatment have adhered to active CNS (Fig. 4(b)). Furthermore, the combination of 2D CNS and 2D MnO_2 nanosheets (Figs. 3(d) and 4(b)) endows the composite more transferring sites for ions on the electrode than those in the MnO_2 granules, notably promoting

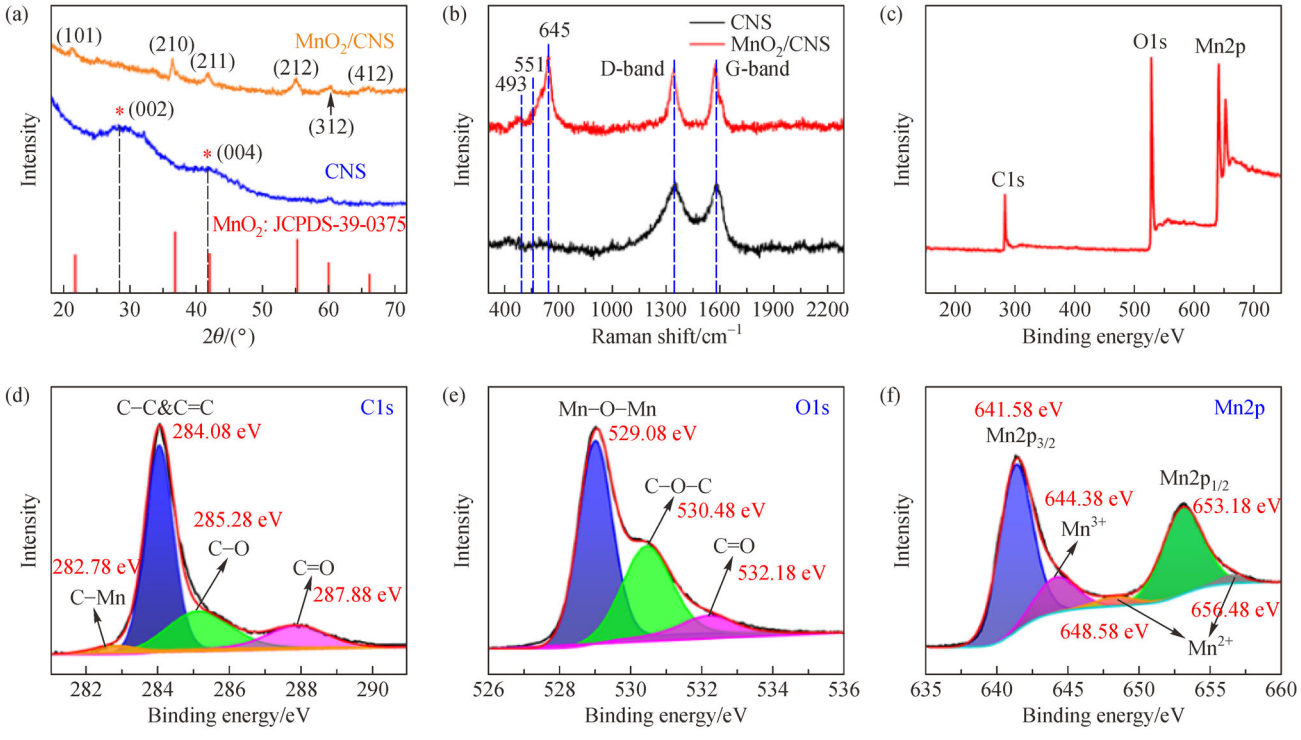

Fig. 2 (a) XRD patterns and (b) Raman spectra of CNS and MnO_2/CNS; (c–f) XPS patterns of MnO_2/CNS: (c) full scans of C, O, and Mn, (d) scan of C1s, (e) O1s, and (f) Mn2p.

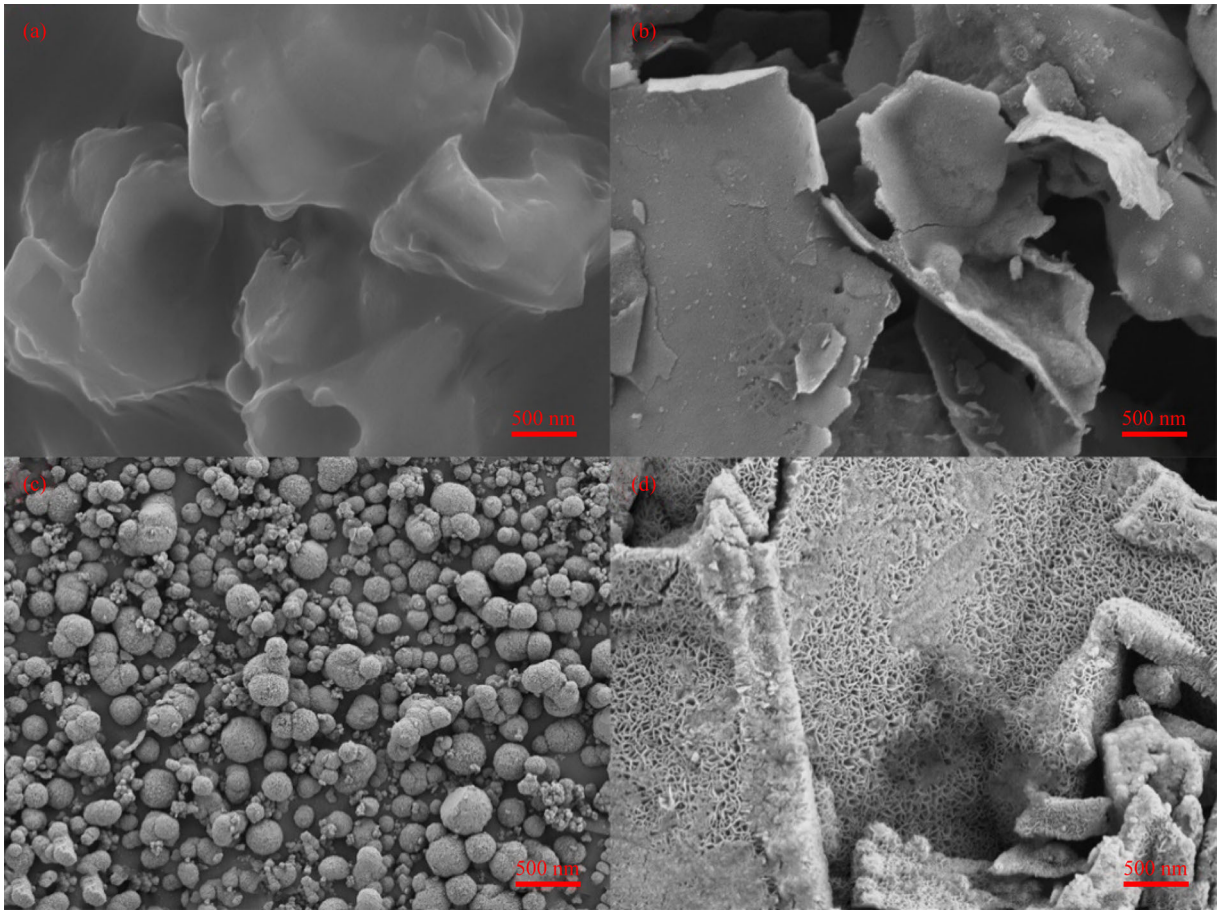

Fig. 3 SEM images of (a) acidless-treated CNS, (b) active CNS, (c) MnO_2, and (d) MnO_2/CNS.

the electrochemical performance of the composite. Figures 4(c) and 4(d) indicate that the active CNS achieves an ultrathin thickness of 1.6 nm.

As shown in Fig. 5, the element distribution in MnO_2/CNS is evaluated with EDS. Three spectra of C, O, and Mn in Figs. 5(b)–5(d) exhibit their homogeneous distribution in MnO_2/CNS.

3.2 Electrochemical performance of electrodes

As shown in Fig. 6, CV, GCD, and EIS were conducted on CNS, MnO_2, and MnO_2/CNS. The CV estimations at a voltage range from –1 to 0.2 V were adopted in the electrolyte of 3 $mol \cdot L^{-1}$ KOH. Figure 6(a) shows the cyclic voltammetry curves of CNS, MnO_2, and MnO_2/CNS at the scan rate of 100 $mV \cdot s^{-1}$, where both oxidation and reduction peaks appear in MnO_2 and MnO_2/CNS at –0.2 V, indicating the apparent reversibility of Faradic reaction in the electrolyte for pseudocapacitor material [30]. Due to the fast insertion and extraction of K-ion that comes from the electrolyte, large quantities of Faradaic reactions take place in the interior and surface of the MnO_2 electrode as follows [31]:

$$MnO_2 + K^+ + e^- = MnOOK \quad (5)$$

MnO_2/CNS possesses a larger curve area than MnO_2, facilitating a much higher electrochemical performance. Figure 6(b) is the GCD curves ranging from –1 to 0.2 V of CNS, MnO_2, and MnO_2/CNS under a basic current density of 1 $A \cdot g^{-1}$. Due to the faradaic reactions of pseudocapacitor material, the curves of MnO_2 and MnO_2/CNS show irregular triangles [32]. The mass-specific capacitance of MnO_2/CNS is higher at 395.5 $F \cdot g^{-1}$ compared with that of MnO_2 (190 $F \cdot g^{-1}$). The composition of CNS significantly enhances the performance of MnO_2, which is attributed to the refined dimensions of MnO_2 when growing on the surface of CNS, the amplified specific surface area, and the prevented agglomeration. When the current density of GCD tests increases to 20 $A \cdot g^{-1}$ (Fig. 6(c)), the mass-specific capacitance of MnO_2/CNS remains 158.2 $F \cdot g^{-1}$, showing a superior rate capability (40%, 158.2/395.5) to that of MnO_2 (11%, 22/190) thanks to the active CNS (44%, 53.7/122 $F \cdot g^{-1}$) as carbon materials always maintain excellent stability under high current density.

The introduction of CNS improves the electrical conductivity of MnO_2/CNS, resulting in much better

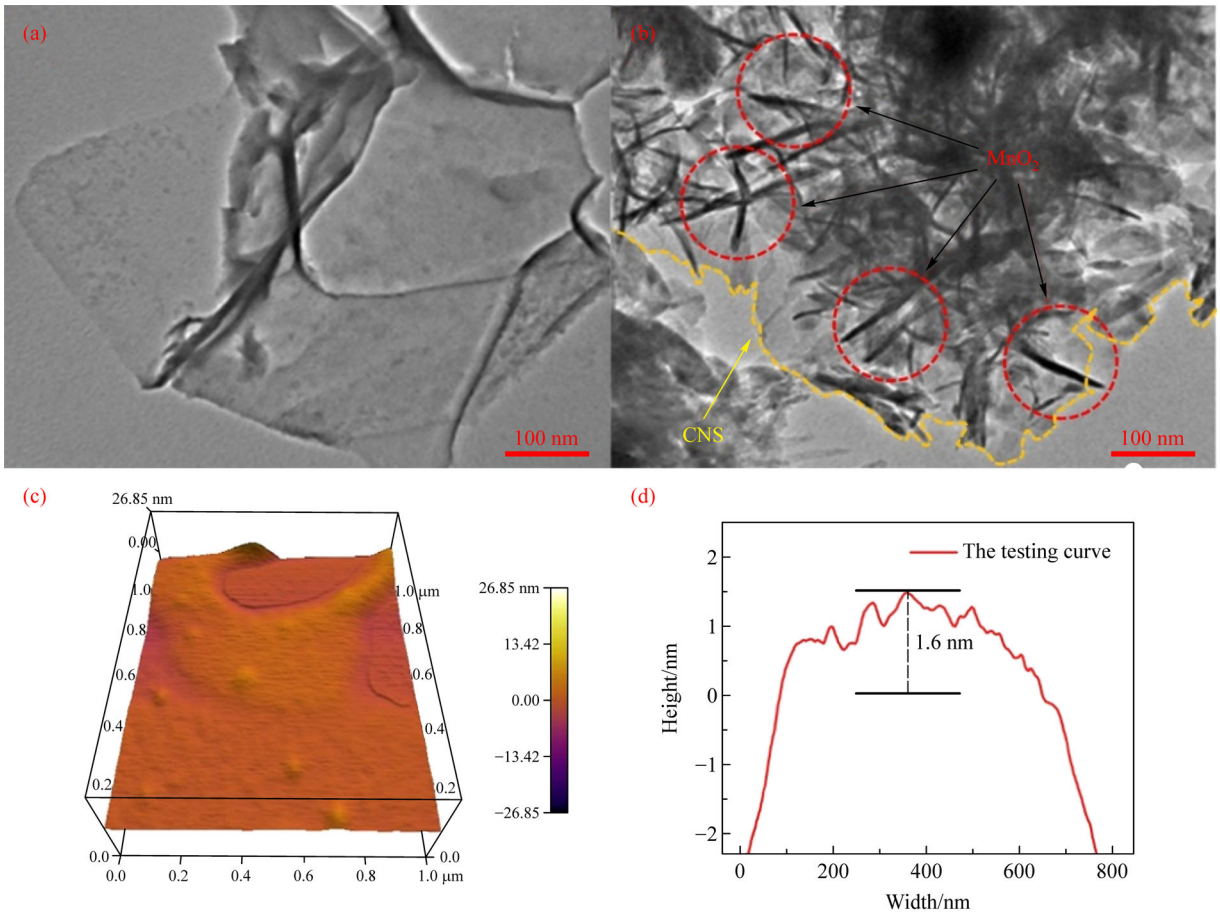

Fig. 4 TEM images of (a) active CNS, and (b) MnO_2/CNS; AFM image of (c) active CNS, and (d) thickness curve for active CNS.

performance than MnO_2, which is also demonstrated with EIS in Fig. 6(d). The Nyquist plot with frequency ranges from 10^{-1} to 10^5 Hz for CNS, MnO_2, and MnO_2/CNS. The Nyquist plot usually consists of the resistive component (Z') of the impedance and the imitate component (Z''), in which the frequency decreases as the profile shifts from the bottom left section to the top right [33]. The Nyquist plot intersects the (Z') axis at the inherent resistance of the electrode, R_S. The smaller the R_S, the better the conductivity. The slope of the oblique line on the plot refers to the resistance derived from the ions transferring between electrode and electrolyte, which is represented by the Warburg element (Z_W). The bigger the Z_W, the better the conductivity [33]. As shown in Fig. 6(d), the intrinsic R_S of MnO_2/CNS is 0.94 Ω, lower than that of MnO_2 (1.04 Ω). The Z_W of MnO_2/CNS is 1.523, which is higher than that of MnO_2 (1.39), indicating the superior conductivity of MnO_2/CNS to raw MnO_2 thanks to the superior conductivity of CNS.

The storage mechanism is investigated to explain the excellent performance of the composite, which is presented in Fig. 7. As shown in Fig. 7(a), a group of CV tests was conducted on MnO_2/CNS with different scan rates ranging from 10 to 100 $mV \cdot s^{-1}$. The relationship between the scan rate (v) and the imported current (i) can be expressed with the appointed power-law [34]:

$$i = av^b, \tag{6}$$

where the slope of the plot, log (v)–log (i), can be written as b. When b approaches 0.5, the electrode charge storage behavior is a battery-type, which emerges with the phase transition during the charging and discharging process. When b is close to 1.0, the charge storage behavior is a double layer capacitor-type, in which the capacitance on the electrode surface relies merely on the physical interactions between electrode and electrolyte [34]. Figure 7(b) is the fitting output originating from the scan rates and current density peaks of anode and cathode. The b values of anode and cathode are 0.524 and 0.852, respectively, proving that the charge storage behavior of MnO_2/CNS is a Faradaic pseudocapacitance-type, which can be generated both on the surface (capacitive behavior) and interior (diffusion behavior) of the electrode. The pseudocapacitor has superior capacitance to the double-layer capacitor. The crystal structure is much more stable than the battery-type materials. $i_c = k_1v + k_2v^{0.5}$ can be

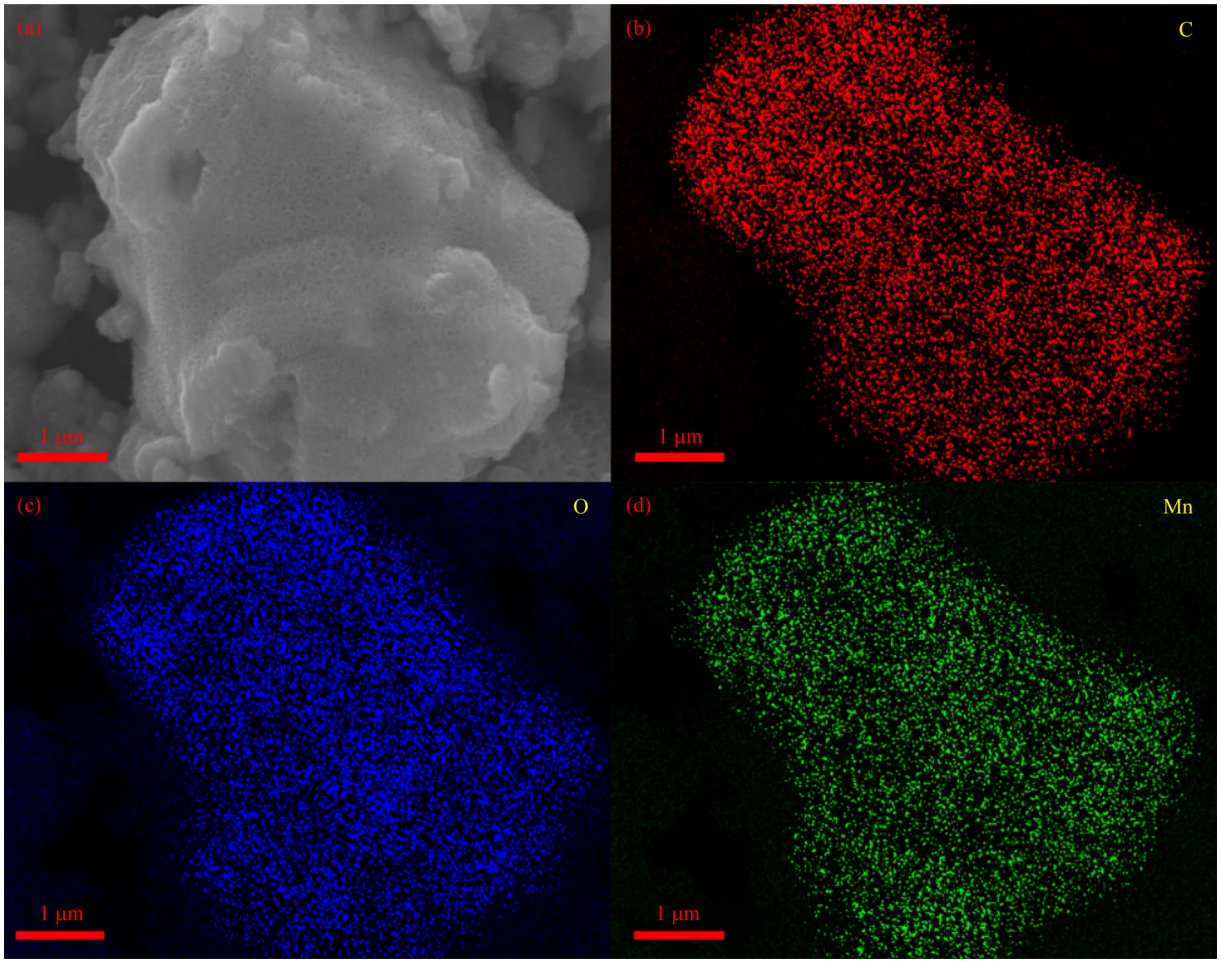

Fig. 5 (a) SEM image of MnO_2/CNS; EDS mappings of (b) C, (c) O, and (d) Mn.

utilized to the capacitance generated by interior diffusion behavior of MnO_2/CNS at different scan rates (v) can be calculated with the following equation [34]:

$$i_c = k_1 v + k_2 v^{0.5}, \tag{7}$$

where i represents the definite total current that corresponds to the tested scan rate (v), and $k_1 v$ and $k_2 v^{0.5}$ are the surface capacitive current and diffusion-controlled current, respectively [34]. As shown in Fig. 7(c), the capacitance of surface behavior at 10 $mV \cdot s^{-1}$ remains 54% of the total value. The proportion of interior diffusion behavior ascends steeply with the increasing scan rate (Fig. 7(d)), accounting for 78% of the whole capacitance at a higher scan rate of 100 $mV \cdot s^{-1}$.

3.3 Electrochemical performance of the ASC

An ASC was assembled, of which the anode was the MnO_2/CNS composite, and the cathode was AC. The loading of AC is calculated based on the charge balance between cathode and anode as follows [35]:

$$\frac{M_+}{M_-} = \frac{C_- \Delta V_-}{C_+ \Delta V_+}, \tag{8}$$

where ΔV_+, C_+, and M_+ are the operating voltage range, the capacitance, and the loading of the anode, respectively, and ΔV_-, C_-, and M_- represent the operating voltage range, the capacitance, and the loading of the cathode, respectively [35]. According to Eq. (8), AC mass loading was calculated to be 3.51 $mg \cdot cm^{-2}$.

As presented in Fig. 8, to evaluate the performance of the ASC of MnO_2/CNS//AC (Fig. 8(a)), CV and GCD were performed. Figure 8(b) presents the CV testing profiles of the supercapacitor under the same scan rate of 100 $mV \cdot s^{-1}$, ranging from 1.0 to 1.8 V, all of which manifested similar shapes, significantly overlapped from 0 to 1.0 V. The asymmetric profiles of CV testing are attributed to the asymmetric structure of the anode and the cathode. Figure 8(c) shows the GCD curves of the supercapacitor under the basic current density of 1 $A \cdot g^{-1}$, ranging from 1.0 to 1.6 V. As shown in Figs. 8(b) and 8(c), the capacitance of the device increases significantly with the voltage, presenting an effective peak of 114.35 $F \cdot g^{-1}$ at

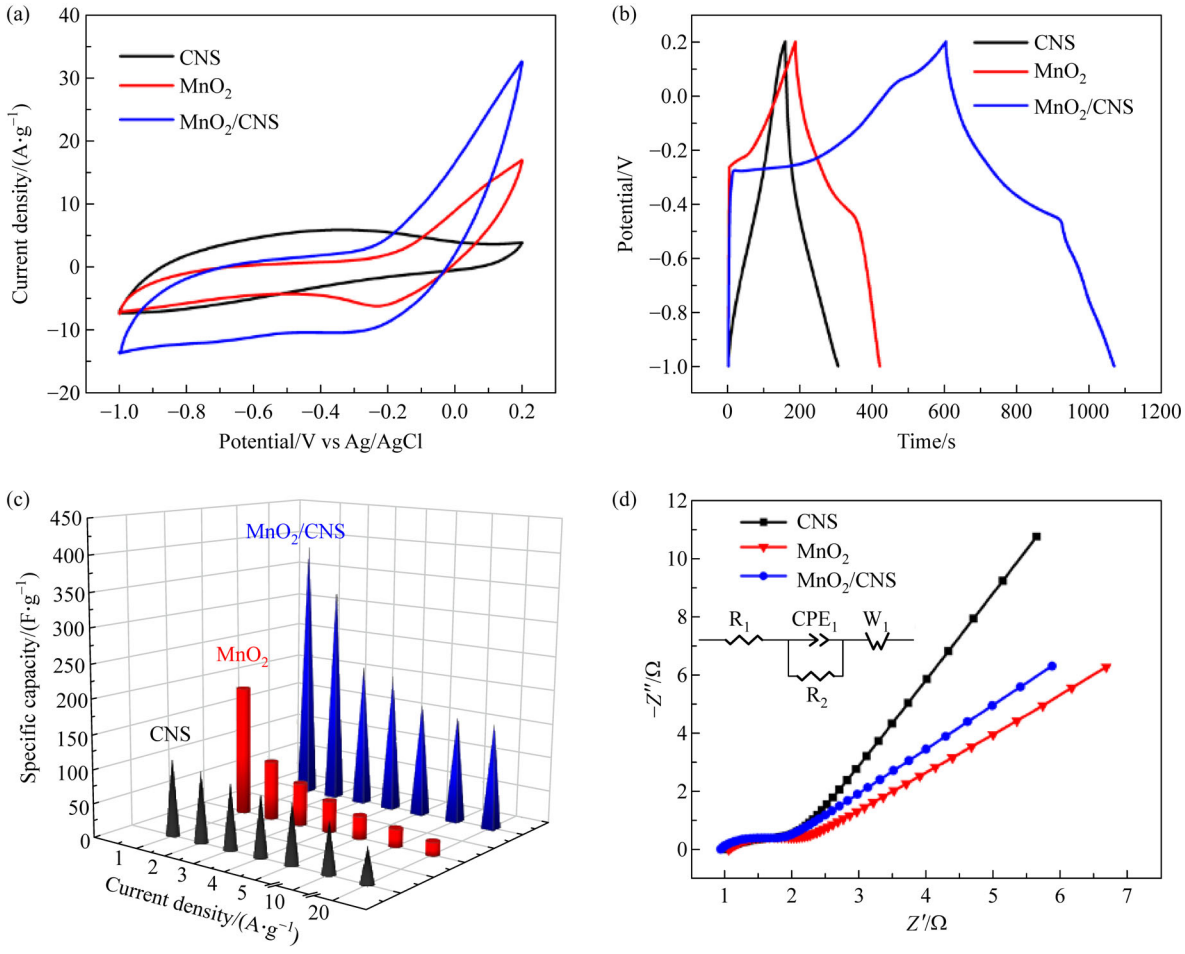

Fig. 6 (a) CV curves of CNS, MnO_2, and MnO_2/CNS at the scan rate of 100 $mV \cdot s^{-1}$; (b) GCD curves of CNS, MnO_2 and MnO_2/CNS at the current density of 1 $A \cdot g^{-1}$; (c) rate capabilities and (d) Nyquist plots of CNS, MnO_2 and MnO_2/CNS.

1.6 V. Meanwhile, the effects of two supercapacitors in series and in paralleled (Fig. 8(d)) on the current and potential window were evaluated. The CV curves are shown in Figs. 8(e) and 8(f). Two supercapacitors in series showed double potential window than the single one (Fig. 8(e)), and two supercapacitors in paralleled showed much greater current than the single one (Fig. 8(f)). The results above are consistent with the electrical regulations in which supercapacitors in series amplify the working potential, and supercapacitors in paralleled broaden the working current, authenticating the feasibility of the supercapacitor [36–38].

CV and GCD tests were also performed to investigate the property of one single supercapacitor, as shown in Fig. 9. The CV curves (Fig. 9(a)) at the increasing scan rates from 10 to 100 $mV \cdot s^{-1}$ showed similar trends with the scan rate. Significantly, the curve at 100 $mV \cdot s^{-1}$ had much more area than those at other scan rates. Different current densities were adopted in the GCD tests to evaluate the supercapacitor rate capability, as shown in Figs. 9(b) and 9(c). The supercapacitor specific capacitances are 114.35, 140.8, 150.9, 153.8, 84.75, and 73.5 $F \cdot g^{-1}$ at the current density of 1, 2, 3, 4, 5, 10 $A \cdot g^{-1}$, respectively. Activated in the durative testing from the previous current densities, the ions on the electrode have the best reaction kinetics at 4 $A \cdot g^{-1}$, facilitating the optimum specific capacitance of 153.8 $F \cdot g^{-1}$. The supercapacitor retains 64% of the specific capacitance calculated at 1 $A \cdot g^{-1}$, while the current density increases to 10 $A \cdot g^{-1}$, showing outstanding rate capability. The ion transfer rate increases as the current density increases, promoting the energy storing and releasing efficiency of the charging and discharging processes. The supercapacitor coulombic efficiency (Fig. 9(c)) reaches up to 97% at the current density of 10 $A \cdot g^{-1}$.

Finally, Fig. 10 presents the practical application of the supercapacitor. The Ragone plot was adopted as the criteria for evaluating its energy density and power density. Dots situated in the top right corner of the chart illustrate the outstanding electrochemical performance [39,40]. The energy density and power density of a supercapacitor can be calculated with the following equations [41]:

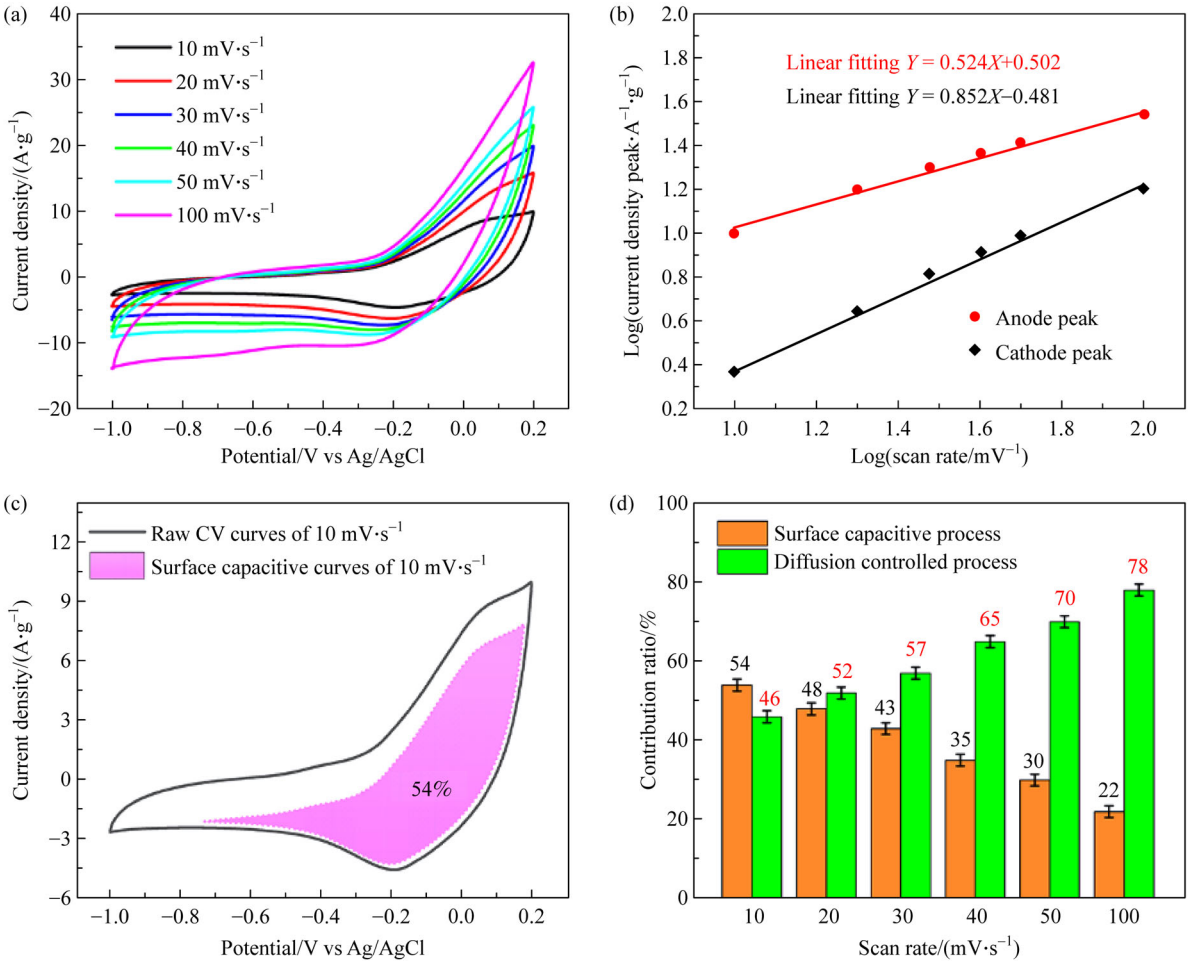

Fig. 7 (a) CV curves of MnO_2/CNS at different scan rates; (b) plots of log (scan rate) versus log (peak current); (c) surface capacitive CV curves of 10 mV·s^{-1}; (d) contribution ratios of surface capacitive and diffusion-controlled process at different scan rates.

$$E = \frac{C \times \Delta V^2}{2 \times 3.6}, \tag{9}$$

$$P = \frac{E \times 3600}{T}, \tag{10}$$

where C refers to the specific capacitance (F/g), ΔV represents the operating potential window (V), and T is the discharging period (s). As presented in Fig. 10(a), the optimal energy density is 54.68 Wh·kg^{-1} at the current density of 4 A·g^{-1}, while the power density is 2559.8 W·kg^{-1}. As the current density increases, the power density reaches the peak of 6399.2 W·kg^{-1} at 10 A·g^{-1}, while the energy density maintains at 26.13 Wh·kg^{-1}, showing the superiority to conventional lead-acid batteries and better electrochemical performance than the those based on MnO_2 (Table 1) [42–49]. Compared with particulate and linear electrode materials, two-dimensional MnO_2 nanosheets are planar, endowing much more space for ion movement and energy storage, protecting the electrode against structure collapse, and improving the energy density and power density of supercapacitors.

Figure 10(b) is the cycling test result of the supercapacitor performed at 4 A·g^{-1}. The supercapacitor retains 75.3% of the initial specific capacitance after 10000 cycles, showing outstanding cycling performance. A significant quantity of ions gradually gathered on the electrode surface during the cycling tests, increasing the R_S and decreasing the Z_w of the supercapacitor (Fig. 10(c)), resulting in inferior properties. Two of the assembled ASCs in series could power a yellow LED with an operating voltage of 2 V for 2 min charging for 3 min (Fig. 10(d)). The application of carbon materials and MnO_2 in the energy storage field is promising.

4 Conclusions

In this work, a low-cost, high capacitance electrode based on MnO_2/CNS was prepared. After the carbonization of tripotassium citrate monohydrate and HNO_3 acidification, CNS was produced, which regulated the magnitude of

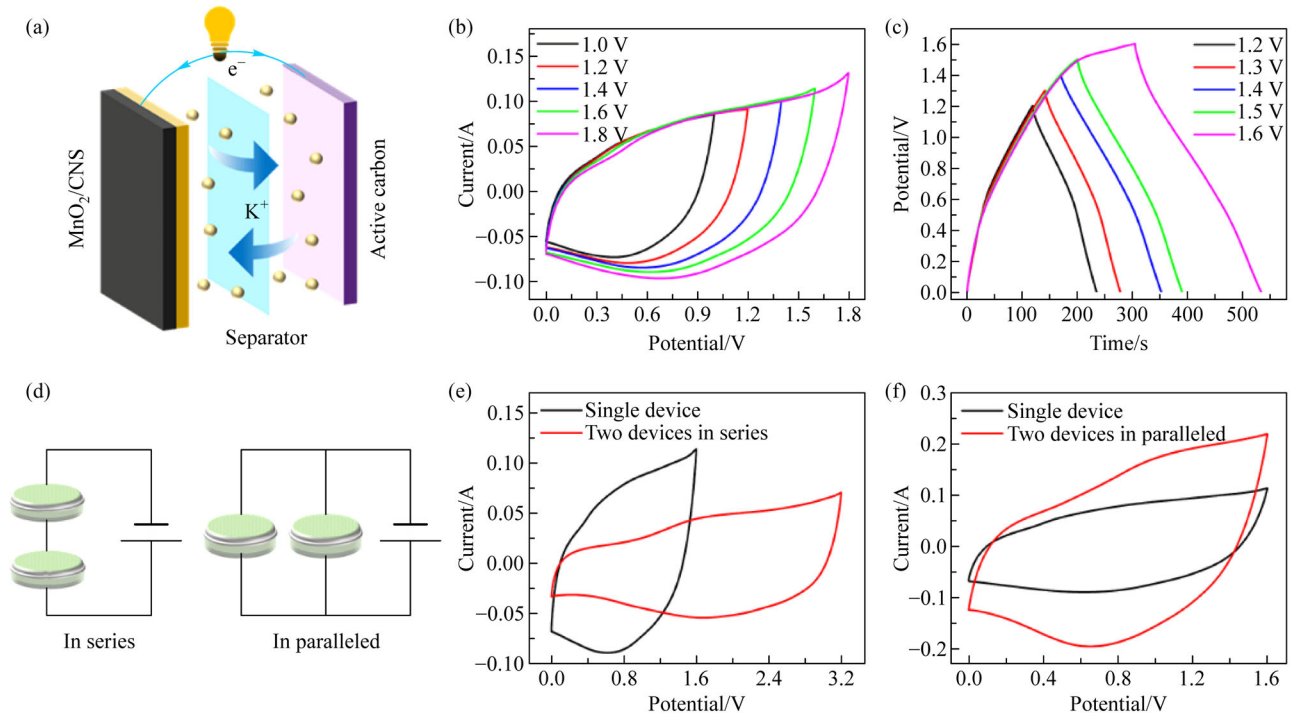

Fig. 8 (a) Schematic diagrams of ASC; (b) CV curves of ASC from 1.0 to 1.8 V at the scan rate of 100 $mV \cdot s^{-1}$; (c) GCD profiles of ASC from 1.0 to 1.6 V at the current density of 1 $A \cdot g^{-1}$; (d) schematic diagrams of two devices in series and in paralleled; CV curves of one device and two devices (e) in series and (f) in paralleled.

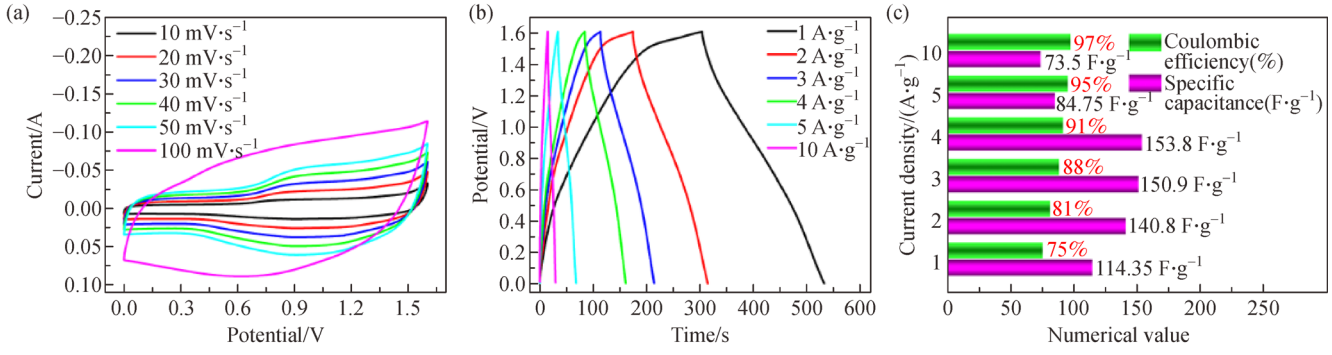

Fig. 9 (a) CV curves of ASC at different scan rates; (b) GCD profiles of ASC at different current densities; (c) rate capability and coulombic efficiency of ASC.

MnO_2 nanosheets grown on its surface while avoiding MnO_2 inhomogeneous dimensions and severe agglomeration. HNO_3 activation provided the large quantities of functional groups for the combination of CNS and MnO_2 nanosheets and promoted the reproduction of MnO_2 on it. The corporation of 2D CNS and 2D MnO_2 nanosheets endowed the composite with plenty of transferring and reacting sites for the ions from the electrolyte, improving the composite electrochemical performance. With excellent conductivity and stability of CNS under strong current, the composite showed a higher rate capability than MnO_2. The $K_3C_6H_5O_7 \cdot H_2O$ derived ultrathin CNS is conducive to the MnO_2/CNS electrode performance. Lastly, an ASC with AC as the cathode and MnO_2/CNS as the anode was successfully assembled, reaching an energy density of 54.68 $Wh \cdot kg^{-1}$ and a power density of 6399.2 $W \cdot kg^{-1}$ superior to conventional lead-acid batteries. After 10000 cycles, the supercapacitor retained 75.3% of the initial capacitance. Successfully powering a LED demonstrated the practical application of the supercapacitor.

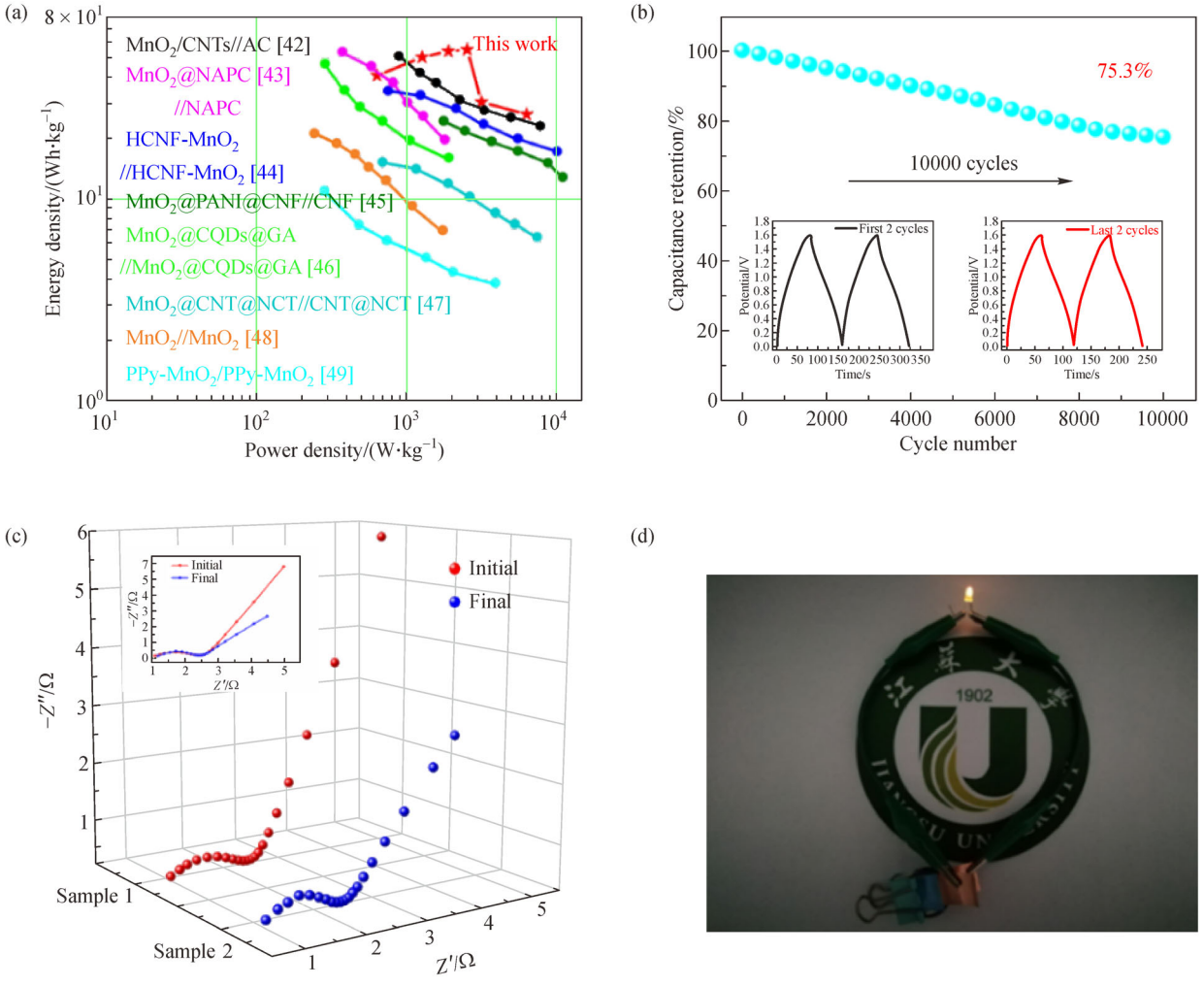

Fig. 10 (a) Ragone plot of ASC; (b) cyclic testing of ASC; (c) Nyquist plots of ASC before and after cycle testing; (d) two devices linked in series light a LED of 2 V.

Table 1 Comparison of ASCs based on MnO_2/CNS//AC with the reported ASCs based on MnO_2 in terms of the maximum for energy density (E) and power density (P) [42–49].

Electrode Material	Electrolyte	Potential window	E/(Wh·kg^{-1})	P/(W·kg^{-1})	Ref.
MnO_2/CNS//AC	3 mol·L^{-1} KOH	0–1.6 V	54.68	6399.2	This work
MnO_2/CNTs//AC	1 mol·L^{-1} Na_2SO_4	0–1.5 V	13.3	600	[42]
MnO_2@N-APC//NAPC	1 mol·L^{-1} Na_2SO_4	0–2 V	28	560	[43]
HCNF-MnO_2//HCNF-MnO_2	PVA-Na_2SO_4	0–1.6 V	30.5	3090	[44]
MnO_2@PANI@CNF//CNF	1 mol·L^{-1} H_2SO_4	–0.5–1.6 V	43	1650	[45]
MnO_2@CQDs@GA//MnO_2@CQDs@GA	1 mol·L^{-1} Na_2SO_4	0–2 V	38.2	1000	[46]
MnO_2@CNT@NCT//CNT@NCT	PVA-Na_2SO_4	0–1.8 V	5.5	3600	[47]
MnO_2//MnO_2	PVA-Na_2SO_4	0–1.6 V	32	1390	[48]
PPy-MnO_2//PPy-MnO_2	PVA-Na_2SO_4	0–1.2 V	37.63	830	[49]

Acknowledgements This work is financially supported by Six Talents Peak Project in Jiangsu Province (Grant No. 2011-ZBZZ045), Key R&D Program of Zhenjiang (Grant No. GY2018016), and Innovative Training Program in Jiangsu University (Grant No. Y18A017).

References

1. Zhang L, Hu X S, Wang Z P, Sun F C, David G D. A review of supercapacitor modeling, estimation, and applications: a control/management perspective. Renewable & Sustainable Energy Reviews, 2018, 81: 1868–1878
2. Poonam K, Sharma K, Arora A, Tripathi S K. Review of supercapacitors: materials and devices. Journal of Energy Storage, 2019, 21: 801–825
3. Yang P, Mai W. Flexible solid-state electrochemical supercapacitors. Nano Energy, 2014, 8: 274–290
4. Gou Q Z, Zhao S, Wang J C, Li M, Xue J M. Recent advances on boosting the cell voltage of aqueous supercapacitors. Nano-Micro Letters, 2020, 12(1): 1–22
5. Béguin F, Presser V, Balducci A, Frackowiak E. Carbons and electrolytes for advanced supercapacitors. Advanced Materials, 2014, 26(14): 2219–2251
6. Yan J, Qian W, Tong W, Fan Z. Recent advances in design and fabrication of electrochemical supercapacitors with high energy densities. Advanced Energy Materials, 2014, 4(4): 1300816
7. Baumann D, Lee C, Wan C Z, Sun H T, Duan X F. Hierarchical porous carbon derived from covalent triazine frameworks for high mass loading supercapacitors. ACS Materials Letters, 2019, 1(3): 320–326
8. Wang Q S, Zhang Y F, Jiang H M, Meng C G. *In-situ* grown manganese silicate from biomass-derived heteroatom-doped porous carbon for supercapacitors with high performance. Journal of Colloid and Interface Science, 2019, 534: 142–155
9. Wang Q S, Zhang Y F, Jiang H M, Li X J, Cheng Y, Meng C G. Designed mesoporous hollow sphere architecture metal (Mn, Co, Ni) silicate: a potential electrode material for flexible all solid-state asymmetric supercapacitor. Chemical Engineering Journal, 2019, 362: 818–829
10. Jiang H M, Zhang Y F, Wang C, Wang Q S, Meng C G, Wang J. Rice husk-derived Mn_3O_4/manganese silicate/C nanostructured composites for high-performance hybrid supercapacitors. Inorganic Chemistry Frontiers, 2019, 6(10): 2788–2800
11. Dong X Y, Zhang Y F, Chen Q, Jiang H M, Wang Q S, Meng C G, Kou Z K. Ammonia-etching-assisted nanotailoring of manganese silicate boost faradic capacity for high-performing hybrid supercapacitors. Sustainable Energy & Fuels, 2020, 4(5): 2220–2228
12. Zhang Y F, Wang C, Dong X Y, Jiang H M, Hu T, Meng C G, Huang C. Alkali etching metal silicates derived from bamboo leaves with enhanced electrochemical properties for solid-state hybrid supercapacitors. Chemical Engineering Journal, 2021, 417: 127964
13. Li Y, Huang D F, Shen W J. Preparation of supercapacitors based on nanocomposites films of MnO_2/CB/C from sodium alginate and MnO_2 nanoparticles by direct electrophoretic deposition and carbonization. Electrochimica Acta, 2015, 182: 104–112
14. Wang Y Q, Wang S S, Wu Y J, Zheng Z M, Hong K Q, Li B S, Sun Y M. Polyhedron-core/double-shell CuO@C@MnO_2 decorated nickel foam for high performance all-solid-state supercapacitors. Electrochimica Acta, 2017, 246: 1065–1074
15. Gu Y J, Wen W, Wu J M. Wide potential window TiO_2@carbon cloth and high capacitance MnO_2@carbon cloth for the construction of a 2.6 V high-performance aqueous asymmetric supercapacitor. Journal of Power Sources, 2020, 469: 228425
16. Zhou H Y, Zhe Y, Yang X, Lv J, Kang L P, Liu Z H. RGO/MnO_2/polypyrrole ternary film electrode for supercapacitor. Materials Chemistry and Physics, 2016, 177: 40–47
17. Wang H J, Peng C, Zheng J D, Peng F, Yu H. Design, synthesis and the electrochemical performance of MnO_2/C@CNT as supercapacitor material. Materials Research Bulletin, 2013, 48(9): 389–3393
18. Noh J C, Yoon C M, Kim Y K, Jang J. High performance asymmetric supercapacitor twisted from carbon fiber/MnO_2 and carbon fiber/MoO_3. Carbon, 2017, 116: 470–478
19. Prasath A, Athika M, Duraisamy E, Sharm A S, Elumalai P. Carbon-quantum-dot-derived nanostructured MnO_2 and its symmetrical supercapacitor performances. ChemistrySelect, 2018, 3(30): 8713–8723
20. Liu S L, Wan K N, Zhang C, Liu T X. Polyaniline-decorated 3D carbon porous network with excellent electrolyte wettability and high energy density for supercapacitors. Composites Communications, 2021, 24: 100610
21. Li L, Chen C, Xie J, Shao Z H, Yang F X. The preparation of carbon nanotube/MnO_2 composite fiber and its application to flexible micro-supercapacitor. Journal of Nanomaterials, 2013, 32: 209–214
22. Liew S Y, Walsh D A, Thielemans W. High total-electrode and mass-specific capacitance cellulose nanocrystal-polypyrrole nanocomposites for supercapacitors. RSC Advances, 2013, 3(24): 9158–9162
23. Fan H S, Zhao N, Wang H, Xu J, Pan F. 3D conductive network-based free-standing PANI-RGO-MWNTs hybrid film for high-performance flexible supercapacitor. Journal of Materials Chemistry. A, Materials for Energy and Sustainability, 2014, 2(31): 12340–12347
24. Wang H L, Xu Z W, Li Z, Cui K, Ding J, Kohandehghan A, Tan X H, Zahiri B, Olsen B C, Holt C M B, David M. Hybrid device employing three-dimensional arrays of MnO in carbon nanosheets bridges battery-supercapacitor divide. Nano Letters, 2014, 14(4): 1987–1994
25. Zhao K M, Xu Z Q, He Z, Ye G Y, Gan Q M, Zhou Z, Liu S Q. Vertically aligned MnO_2 nanosheets coupled with carbon nanosheets derived from Mn-MOF nanosheets for supercapacitor electrodes. Journal of Materials Science, 2018, 53(18): 13111–13125
26. Lang J W, Kong L B, Liu M, Luo Y C, Kang L. Asymmetric supercapacitors based on stabilized α-$Ni(OH)_2$ and activated carbon. Journal of Solid State Electrochemistry, 2010, 14(8): 1533–1539
27. Yan J, Fan Z J, Wei T, Qian W Z, Zhang M L, Wei F. Fast and reversible surface redox reaction of graphene-MnO_2 composites as supercapacitor electrodes. Carbon, 2010, 48(13): 3825–3833
28. Dong X C, Wang X W, Wang J, Song H, Li X G, Wang L H, Park M B C, Li C M, Chen P. Synthesis of a MnO_2-graphene foam hybrid with controlled MnO_2 particle shape and its use as a supercapacitor

electrode. Carbon, 2012, 50(13): 4865–4870
29. Li Z P, Mi Y J, Liu X H, Liu S, Yang S R, Wang J Q. Flexible graphene/MnO_2 composite papers for supercapacitor electrodes. Journal of Materials Chemistry, 2011, 21(38): 14706–14711
30. Lei Z B, Shi F H, Lu L. Incorporation of MnO_2-coated carbon nanotubes between graphene sheets as supercapacitor electrode. ACS Applied Materials & Interfaces, 2012, 4(2): 1058–1064
31. Mao L, Zhang K, Chan H S O, Wu J S. Nanostructured MnO_2/graphene composites for supercapacitor electrodes: the effect of morphology, crystallinity and composition. Journal of Materials Chemistry, 2012, 22(5): 1845–1851
32. Yu L, Zhang G Q, Yuan C Z, Lou X W. Hierarchical $NiCo_2O_4$@MnO_2 core-shell heterostructured nanowire arrays on Ni foam as high-performance supercapacitor electrodes. Chemical Communications, 2013, 49(2): 137–139
33. Zhang J W, Dong L B, Xu C J, Hao J W, Kang F Y, Li J. Comprehensive approaches to three-dimensional flexible supercapacitor electrodes based on MnO_2/carbon nanotube/activated carbon fiber felt. Journal of Materials Science, 2017, 52(10): 5788–5798
34. Li Y, Chen C. Polyaniline/carbon nanotubes-decorated activated carbon fiber felt as high-performance, free-standing and flexible supercapacitor electrodes. Journal of Materials Science, 2017, 52 (20): 12348–12357
35. Yue S F, Ma L, Xu B, Chu L. Activated carbon fiber felt used directly as electrode for supercapacitor. Dianchi, 2011, 41(02): 62–65
36. Jiang H, Yan X H, Miao J Y, You M Y, Zhu Y H, Pan J M, Wang L, Cheng X N. Super-conductive silver nanoparticles functioned three-dimensional Cu_xO foams as a high-pseudocapacitive electrode for flexible asymmetric supercapacitors. Journal of Materiomics, 2021, 7(1): 156–165
37. Mathis T S, Kurra N, Wang X H, Pinto D, Simon P, Gogotsi Y. Energy storage data reporting in perspective-guidelines for interpreting the performance of electrochemical energy storage systems. Advanced Energy Materials, 2019, 9(39): 1902007
38. Jiang H, Zhou C, Yan X H, Miao J Y, You M Y, Zhu Y H, Li Y L, Zhou W D, Cheng X N. Effects of various electrolytes on the electrochemistry performance of Mn_3O_4/carbon cloth to ultra-flexible all-solid-state asymmetric supercapacitor. Journal of Energy Storage, 2020, 32: 101898
39. Gao L J, Peng A P, Wang Z Y, Zhang H, Shi Z J, Gu Z N, Cao G P, Ding B Z. Growth of aligned carbon nanotube arrays on metallic substrate and its application to supercapacitors. Solid State Communications, 2008, 146(9-10): 380–383
40. Wu Y J, Gao G H, Wu G M. Self-assembled three-dimensional hierarchical porous V_2O_5/graphene hybrid aerogels for supercapacitors with high energy density and long cycle life. Journal of Materials Chemistry. A, Materials for Energy and Sustainability, 2015, 3(5): 1828–1832
41. Vellacheri R, Zhao H P, Mühlstädt M, Ming J, Al-Haddad A, Wu M H, Jandt K D, Lei Y. All-solid-state cable-type supercapacitors with ultrahigh rate capability. Advanced Materials Technologies, 2016, 1 (1): 1600012
42. Li L, Hu Z A, An N, Yang Y Y, Li Z M, Wu H Y. Facile synthesis of MnO_2/CNTs composite for supercapacitor electrodes with long cycle stability. Journal of Physical Chemistry C, 2014, 118(40): 22865–22872
43. Li D Y, Lin J, Lu Y, Huang Y, He X, Yu C, Zhang J, Tang C C. MnO_2 nanosheets grown on *N*-doped agaric-derived three-dimensional porous carbon for asymmetric supercapacitors. Journal of Alloys and Compounds, 2019, 815: 152344
44. Raza F, Ni X P, Wang J Q, Liu S F, Jiang Z, Liu C L, Chen H F, Farooq A, Ju A Q. Ultrathin honeycomb-like MnO_2 on hollow carbon nanofiber networks as binder-free electrode for flexible symmetric all-solid-state supercapacitors. Journal of Energy Storage, 2020, 30: 101467
45. Dirican M, Yanilmaz M, Asiri A M, Zhang X W. Polyaniline/MnO_2/porous carbon nanofiber electrodes for supercapacitor. Journal of Electroanalytical Chemistry (Lausanne, Switzerland), 2020, 861: 113995
46. Lv H P, Yuan Y, Xu Q J, Liu H M, Wang Y G, Xia Y Y. Carbon quantum dots anchoring MnO_2/graphene aerogel exhibits excellent performance as electrode materials for supercapacitor. Journal of Power Sources, 2018, 398: 167–174
47. Wang Y H, Zhang D Y, Lu Y, Wang W X, Peng T, Zhang Y G, Guo Y, Wang Y G, Huo K F, Kim J K, Luo Y S. Cable-like double-carbon layers for fast ion and electron transport: an example of CNT@NCT@MnO_2 3D nanostructure for high-performance supercapacitors. Carbon, 2018, 143: 335–342
48. Das H T, Saravanya S, Elumalai P. Disposed dry cells as sustainable source for generation of few layers of graphene and manganese oxide for solid-state symmetric and asymmetric supercapacitor applications. ChemistrySelect, 2018, 3(46): 13275–13283
49. Bai M H, Liu R, Yang X B, Yu Z, Wang Y, Zhao Z. Polypyrrole and manganese oxide composite materials with high working voltage and excellent cycling stability. ChemistrySelect, 2018, 3(38): 10574–10579